

# Double- $Q$ spin chirality stripes in the anomalous Hall antiferromagnet $\text{CoNb}_3\text{S}_6$

B. Zager,<sup>1</sup> R. Fan,<sup>2</sup> P. Steadman,<sup>2</sup> and K. W. Plumb<sup>1,\*</sup>

<sup>1</sup>*Department of Physics, Brown University, Providence, Rhode Island 02912, USA*

<sup>2</sup>*Diamond Light Source Ltd., Harwell Science and Innovation Campus, Didcot OX11 0DE, United Kingdom*  
(Dated: July 11, 2023)

The metallic antiferromagnet  $\text{CoNb}_3\text{S}_6$  exhibits a giant anomalous Hall effect (AHE) that cannot be explained by a collinear Néel order on intercalated Co ions. Thus, a noncoplanar structure is expected. We carried out resonant elastic x-ray scattering (REXS) to reexamine the magnetic structure of  $\text{CoNb}_3\text{S}_6$  and found a double- $Q$  ( $2Q$ ) order with a  $(\frac{1}{2}00)$  commensurate component and a long-wavelength modulation. Circular dichroism and linear polarization analysis reveal that the commensurate components on the two Co sites are noncollinear and the modulation is helical. The resulting magnetic structure has a staggered scalar spin chirality forming a stripe pattern in real space. Furthermore, we found that the helical modulation wavevector exhibits a sample dependence and develops a low-symmetry domain structure. We propose that quenched-in lattice strain controls the helical domain structure, accounting for much of the sample dependence. These results provide insight into the mechanism of the AHE in  $\text{CoNb}_3\text{S}_6$  and identifies potential routes for controlling the Hall response and realizing other unconventional electronic phenomena in metallic antiferromagnets.

Materials with complex magnetic phases beyond traditional ferro- and antiferromagnetism exhibit a diverse range of phenomena that are both fundamentally rich and offer many potential applications as next-generation electronic and spintronic devices. Such phases include noncoplanar, chiral, and topological spin textures [1, 2], altermagnetism [3, 4], multiferroics [5], and multipolar magnetism [6]. In these materials, the intricate magnetic symmetries allow for the coupling between charge, magnetic, and lattice degrees of freedom from which effective composite degrees of freedom emerge and give rise to novel macroscopic response.

Transition metal dichalcogenides intercalated with  $3d$  transition metal ions form a class of materials where such complex magnetic phases are stabilized through an interplay between localized spins on the  $3d$  sites and itinerant electrons in the host layers [7, 8]. Diverse phenomena are possible depending on the host compound, intercalation species, and intercalation ratio. Co-intercalated  $\text{NbS}_2$ ,  $\text{CoNb}_3\text{S}_6$ , is of particular interest because it exhibits a giant anomalous Hall effect (AHE) that cannot be explained by its reported collinear antiferromagnetic structure [9–11]. A series of neutron diffraction measurements have found the symmetry-related magnetic propagation vectors  $(\frac{1}{2}00)$ ,  $(0\frac{1}{2}0)$ , and  $(\frac{1}{2}\frac{1}{2}0)$ , but disagree on the orientation of the moments and the presence of single- $Q$  domains or multi- $Q$  order [10–14]. Elucidating the precise details of the magnetic structure is an essential step towards understanding the origin of the giant AHE in this antiferromagnet, and potentially tuning the properties to realize new functionalities.

In this letter, we reexamine the magnetic structure of  $\text{CoNb}_3\text{S}_6$  using Co  $L_3$  edge resonant elastic x-ray scattering (REXS). We find a double- $Q$  ( $2Q$ ) magnetic structure with a commensurate  $\mathbf{Q}_0 = (\frac{1}{2}00)$  component and incommensurate  $\mathbf{Q}_0 \pm \mathbf{q}$  modulation giving rise to a staggered scalar spin chirality with a modulated stripe or

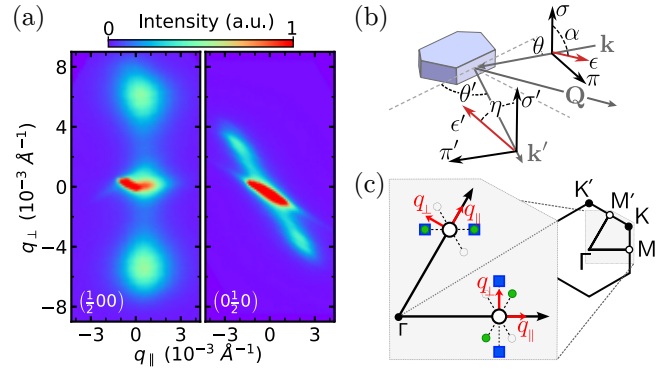


FIG. 1. (a) Magnetic REXS intensity in sample 3 at 16 K using circularly polarized x-rays. (b) Experimental geometry, incident (outgoing) polarization channels  $\sigma$  ( $\sigma'$ ) and  $\pi$  ( $\pi'$ ) correspond to  $\alpha$  ( $\eta$ ) of  $0^\circ$  and  $90^\circ$  respectively. (c) Summary of observed magnetic peaks in the first Brillouin zone across all measured samples. Large white circles are  $\mathbf{Q}_0 = (\frac{1}{2}00)$  and  $(0\frac{1}{2}0)$ , green circles show the magnetic reflections observed in samples 1 and 2 and blue squares show those found in sample 3 as in (a). Dashed lines with empty markers show positions of symmetry allowed peaks that were not observed.

checkerboard pattern. The commensurate component of the structure is noncollinear and the incommensurate component is helical. The data confirms that  $(\frac{1}{2}00)$  and  $(0\frac{1}{2}0)$  peaks belong to separate  $2Q$  domains. Finally, we found that the modulation varies between samples and shows an asymmetric domain pattern implicating lattice strains to influence the magnetic structure, and likely the anomalous Hall response of  $\text{CoNb}_3\text{S}_6$ .

Single crystals were grown using chemical vapor transport [9] with the nominal stoichiometry  $\text{Co:Nb:S}=1:3:6$ . Four different samples from the same growth were measured. All samples undergo abrupt magnetic transitions at 28.6 K, and exhibit sharp (100)-type Bragg peaks, indicating a well-ordered triangular lattice of intercalated

Co ions [15, 16]. REXS experiments were performed at the I10 beamline at Diamond Light Source using the RASOR endstation [17] with the experimental geometry shown in Fig. 1(b). Samples were mounted in the  $(HK0)$  scattering plane to access  $(\frac{1}{2}00)$  and  $(0\frac{1}{2}0)$  magnetic wavevectors at  $2\theta = 106.2^\circ$  at the Co  $L_3$  edge (778.5 eV). In this geometry the x-ray beam scatters from a  $(110)$  facet probing an effective area of  $20 \times 200 \mu\text{m}$ , and with a penetration depth of  $0.3 \mu\text{m}$ . Thus, our measurements probe a macroscopic sample volume containing many basal plane layers. Data was collected for four different samples using an area detector and full linear polarization analysis (FLPA) was carried out on a fifth sample using a point detector and multilayer polarization analyzer optimized for the Co  $L_3$  edge [18]. Measurements were performed for zero-field-cooling (ZFC) and field-cooling (FC) under the application of a 0.1 T permanent magnet along the  $(001)$  direction.

Representative reciprocal space maps of the magnetic scattering are shown in Fig. 1(a). Primary magnetic reflections at  $\mathbf{Q}_0 = (\frac{1}{2}00)$  and  $(0\frac{1}{2}0)$  were observed in all samples, consistent with previous reports [11]. Our fine resolution measurements also revealed a long-wavelength incommensurate modulation of the magnetic structure through satellite magnetic reflections at  $\mathbf{Q}_0 \pm \mathbf{q}$  [Fig. 1]. These satellites showed three distinct behaviors between samples as summarized in Fig. 1(b). In samples 1 and 2, satellites appear at  $(\frac{1}{2}, \pm\delta, 0)$  and  $(\pm\delta, \frac{1}{2}, 0)$ , in sample 3 one set of satellites appears at  $(\pm\delta, \frac{1}{2}, 0)$  while the other set appears at  $(\frac{1}{2} \mp \delta, \pm 2\delta, 0)$ , i.e. purely transverse to the main peak. No satellite reflections were observed in sample 4 [15]. At  $T = 14$  K, we find  $\delta = 3.0(3) \times 10^{-3}$  r.l.u. =  $3.7(3) \times 10^{-3} \text{ \AA}^{-1}$ , corresponding to a modulation with 170(15) nm wavelength, or 97(10) nm for sample 3  $(\frac{1}{2}00)$ . These results were consistent across multiple zero-field-cooled (ZFC) and field-cooled (FC) cycles.

The different satellite wavevectors that appear between  $(\frac{1}{2}00)$  and  $(0\frac{1}{2}0)$  reflections in sample 3 [Fig. 1(a)] break both  $C_6$  rotational and mirror symmetry about  $(110)$  of the triangular lattice, while the satellite reflections observed in samples 1 and 2 possess mirror symmetry but break the  $C_6$  rotational symmetry. Such symmetry reductions indicate that  $(\frac{1}{2}00)$  and  $(0\frac{1}{2}0)$  belong to distinct domains, not a single multi- $Q$  domain, as will be further confirmed by the linear polarization analysis presented below. In this case, the particular long wavelength modulation of the magnetic structure realized in each domain of a given sample may be selected through a symmetry-breaking field such as small lattice strains that are quenched in during crystal synthesis.

Fig. 2 shows the temperature-dependent integrated intensities at  $\mathbf{Q}_0 = (\frac{1}{2}00)$  and  $\mathbf{Q}_0 + (\delta \ 2\delta \ 0)$  in sample 3. Both sets of peaks have the same critical temperature of  $T_N = 28$  K and an intensity that varies smoothly with temperature. We also observed a smooth decrease in the

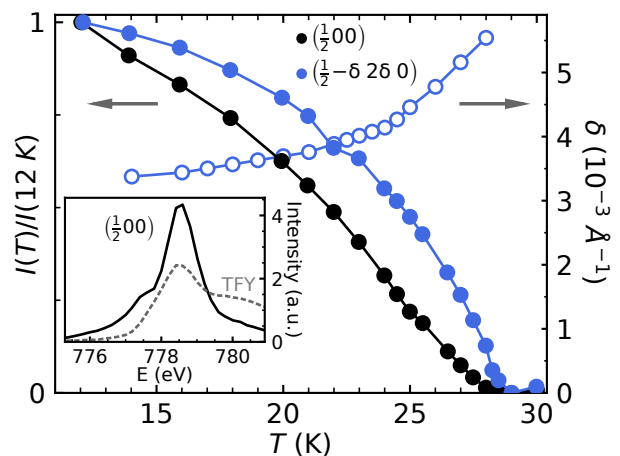


FIG. 2. Normalized temperature dependence of main and satellite peak, and parameter  $\delta$  in satellite wavevector  $(\delta, -2\delta, 0)$  for sample 3 measured on the point detector with  $\pi$  polarized x-rays. The inset shows a fixed- $Q$  energy scan of the main peak, with the dashed line showing total fluorescence yield (TFY).

magnitude of the satellite wave vector with decreasing temperature, decreasing towards  $\mathbf{Q}_0$  as temperature is decreased [Fig. 2], characteristic of a helical magnetic modulation [19]. The spectral lineshape of incident energy scans across the 778.5 eV resonance is typical for  $\text{Co}^{2+}$  [20, 21] and further verifies the magnetic origin of observed peaks [Fig. 2 inset, and Fig. 3 (b) inset].

Further details of the magnetic structure are revealed through the polarization-dependent resonant x-ray scattering. All magnetic reflections exhibit a finite circular dichroism (CD), [Fig. 3], arising at  $\mathbf{Q}_0$  from noncollinearity of the commensurate component, and at  $\mathbf{Q}_0 \pm \mathbf{q}$  from a helical modulation [15]. The CD at  $(\frac{1}{2}00)$  shows a variation along the  $(1\bar{2}0)$  direction suggesting the presence of opposite chirality domains that may have slightly different values of  $\delta$  or are spatially separated on a length scale comparable to the beam size. We also find that the CD varies between ZFC and 0.1 T FC measurements, especially for the  $(\frac{1}{2}00)$  peaks, which is consistent with a redistribution of chiral domains, as we discuss below.

Precise moment directions were determined from full linear polarization analysis (FLPA) by measuring the intensity at  $\mathbf{Q}_0$  as a function of incident polarization angle  $\alpha$  at various fixed analyzer angles  $\eta$  [Fig. 1(b)]. The polarization-dependent intensity shown in Fig. 4(a) is directly sensitive to the real space orientations of the Fourier component  $\mathbf{m}_{\mathbf{Q}_0, n}$  of the magnetic moments.

To model the polarization-dependent scattering intensity in  $\text{CoNb}_3\text{S}_6$ , we consider a  $2Q$  magnetic structure with propagation vectors  $\mathbf{Q}_0$  and  $\mathbf{Q}_0 \pm \mathbf{q}$  (See SI [15] for alternate possibilities). The real space form of this

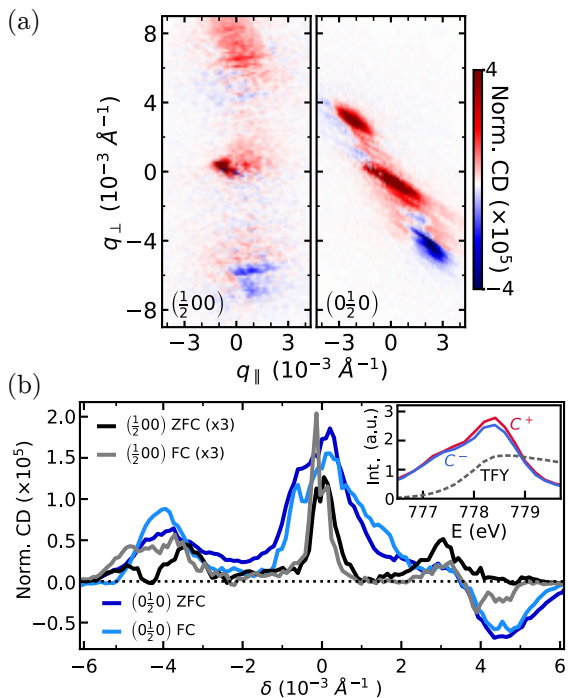


FIG. 3. (a) CD at  $(\frac{1}{2}00)$  and  $(0\frac{1}{2}0)$  for field-cooling (FC). (b) FC vs ZFC Line cuts along  $(\delta, -2\delta, 0)$  at  $(\frac{1}{2}00)$  and along  $(\delta 0 0)$  at  $(0\frac{1}{2}0)$ , averaged over  $0.0025 \text{ \AA}^{-1}$  along the transverse direction. The normalized CD is defined as  $(C^+ - C^-) / \int (C^+ + C^-)$ . Inset shows energy scans at fixed  $\mathbf{Q} = (\frac{1}{2} - \delta, 2\delta, 0)$ .

structure is

$$\begin{aligned} \mathbf{m}_n(\mathbf{r}_j) = & \cos(\mathbf{q} \cdot \mathbf{r}_j + \psi_n) \cos(\mathbf{Q}_0 \cdot \mathbf{r}_j + \phi_n) \hat{\mathbf{u}}_n \\ & + \sin(\mathbf{Q}_0 \cdot \mathbf{r}_j + \phi_n) \hat{\mathbf{v}}_n, \\ & + \cos(\mathbf{q} \cdot \mathbf{r}_j + \psi_n + \frac{\pi}{2}\chi) \cos(\mathbf{Q}_0 \cdot \mathbf{r}_j + \phi_n) \hat{\mathbf{w}}_n, \end{aligned} \quad (1)$$

where  $n=1, 2$  labels the sublattices at 2 Co sites in the unit cell,  $\chi = \pm 1$  is the helix chirality,  $\phi_n$  and  $\psi_n$  are the phases on sublattice  $n$  for  $\mathbf{Q}_0$  and  $\mathbf{Q}_0 \pm \mathbf{q}$  respectively, and  $\hat{\mathbf{u}}_n$ ,  $\hat{\mathbf{v}}_n$ , and  $\hat{\mathbf{w}}_n$  are unit vectors, which we assume to be orthogonal to maintain a constant moment size. The Fourier components of this structure are

$$\begin{aligned} \mathbf{m}_{\mathbf{Q}_0, n} &= \mathbf{m}_{-\mathbf{Q}_0, n}^* = -\frac{i}{2} e^{i\phi_n} \hat{\mathbf{v}}_n \\ \mathbf{m}_{\mathbf{Q}_0 \pm \mathbf{q}, n} &= \mathbf{m}_{-\mathbf{Q}_0 \mp \mathbf{q}, n}^* = \frac{1}{4} e^{i\phi_n \pm i\psi_n} (\hat{\mathbf{u}}_n \pm i\hat{\mathbf{w}}_n). \end{aligned} \quad (2)$$

We parameterize the magnetic structure in terms of the angle  $\mu_n$  of  $\hat{\mathbf{u}}_n$  from the lattice vector  $\mathbf{a}_1 = a\hat{\mathbf{x}}$  within the  $a$ - $b$  plane, out-of-plane canting angle  $\nu_n$  of  $\mathbf{v}_n$ , and phases  $\phi_n$ ,  $\psi_n$ . We fit the commensurate component  $\mathbf{m}_{\mathbf{Q}_0, n}$  to the measured FLPA shown in Fig. 4(a).  $\nu_1 = \nu_2$  is ruled out as this always leads to zero  $\pi$ - $\pi'$  intensity, inconsistent with the observed FLPA and CD. For our analysis, we have fixed  $\mu_1 = \mu_2 = \mu$  and  $\nu_1 = -\nu_2 = \nu$ . We find no improvements in the model by relaxing these constraints.

While the phase variables  $\phi_n$  and  $\psi_n$  cannot be uniquely determined from our measurements, symmetry

TABLE I. Parameters obtained from FLPA describing the commensurate Fourier component, for the two possible choices of  $\Delta\phi$ .

Peak	$\Delta\phi = 0^\circ$		$\Delta\phi = 180^\circ$	
	$\mu$	$\nu$	$\mu$	$\nu$
$(\frac{1}{2}00)$	$109(1)^\circ$	$37(2)^\circ$	$109(1)^\circ$	$14(2)^\circ$
$(0\frac{1}{2}0)$	$12(1)^\circ$	$24(2)^\circ$	$12(1)^\circ$	$9(2)^\circ$

constrains  $\Delta\phi = \phi_2 - \phi_1$  to either  $0^\circ$  or  $180^\circ$  [22]. We separately consider two cases:  $\Delta\phi = 0^\circ$  or  $\Delta\phi = 180^\circ$  and find for both  $\mu = 109(1)^\circ$  at  $(\frac{1}{2}00)$  and  $\mu = 12(1)^\circ$  at  $(0\frac{1}{2}0)$ , or nearly  $\pm 80^\circ$  from  $\mathbf{Q}_0$ . The in-plane angle relative to  $\mathbf{Q}_0$  is opposite in each domain, with the same broken symmetry as the modulation wavevectors in samples 1 and 2 [15]. For  $\Delta\phi = 0^\circ$  we find  $\nu = 37(2)^\circ$  at  $(\frac{1}{2}00)$  and  $\nu = 24(2)^\circ$  at  $(0\frac{1}{2}0)$ . While for  $\Delta\phi = 180^\circ$ , we find  $\nu = 14(2)^\circ$  at  $(\frac{1}{2}00)$  and  $\nu = 9(2)^\circ$  at  $(0\frac{1}{2}0)$ . Both cases adequately describe the data at  $(\frac{1}{2}00)$  while neither fully matches the intensity at  $\pi$ - $\sigma$  for  $(0\frac{1}{2}0)$ . We attribute this discrepancy to an experimental artifact likely due to a slight analyzer misalignment. Furthermore, we cannot rule out contributions from domains with different moment orientations because the x-ray intensity measures an ensemble-average for a given  $\mathbf{Q}$ . The results of our fit are summarized in Table I and Fig. 4(b) shows a real-space representation of the magnetic structure found in sample 3.

Our measurements reveal that  $\text{CoNb}_3\text{S}_6$  hosts a non-coplanar magnetic structure [Fig. 4(d)] that may strongly influence the electronic transport properties. In particular, a nonzero scalar spin chirality,  $\chi_s = \mathbf{m}(\mathbf{r}_i) \cdot [\mathbf{m}(\mathbf{r}_j) \times \mathbf{m}(\mathbf{r}_k)]$  for sites  $i, j, k$  on a triangular plaquette generates an effective magnetic field felt by conduction electrons passing over the plaquette:  $\mathbf{b}_\alpha \propto t_\alpha \chi_{s, \alpha} \hat{\mathbf{n}}_\alpha$ , where  $\hat{\mathbf{n}}_\alpha$  is the plaquette normal vector and  $t_\alpha = t_{ij} t_{jk} t_{ki}$  is the hopping integral around the plaquette [13]. We compute the total scalar spin chirality for  $\text{CoNb}_3\text{S}_6$  using the real space spin structures found above by considering separate contributions from intra-sublattice plaquettes  $\chi_s^\parallel$ , and inter-sublattice plaquettes  $\chi_s^\perp$ , involving two sites from one sublattice and one site from the opposite one [Fig. 4(c)].

We find that the uniform net scalar chirality vanishes  $\chi_s(Q=0) = 0$ , but the local scalar chirality is finite.  $\chi_s^\parallel$  forms stripes with propagation vector  $\mathbf{Q}_0$  and no variation along  $\mathbf{q}$ . The stripes on each sublattice are  $\pm 90^\circ$  out of phase for  $\Delta\phi = 0^\circ$  or  $180^\circ$ .  $\chi_s^\perp$  depends on  $\nu$  and forms complex structures that depend on the choice of the phase variables. We apply the constraint  $\Delta\psi = 0^\circ$  or  $180^\circ$  to consider four different combinations of phases that result in stripe or checkerboard like patterns of chirality [15]. In all cases, the magnitudes of  $\chi_s^\parallel$  and  $\chi_s^\perp$

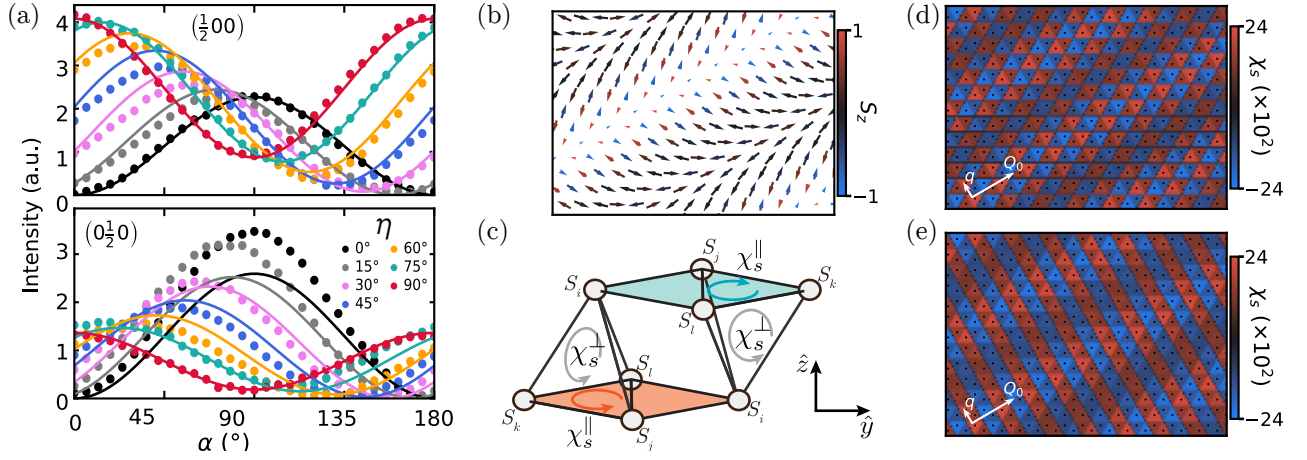


FIG. 4. (a) FLPA data and model at  $(\frac{1}{2}00)$  and  $(0\frac{1}{2}0)$ . (b) Real space depiction of magnetic structure on a single sublattice for  $\mathbf{Q}_0 = (\frac{1}{2}00)$  and  $\mathbf{q} = (-\delta, 2\delta, 0)$ , plotted for  $\delta = 0.053$  r.l.u.,  $\phi = 45^\circ$ ,  $\mu = 110^\circ$ ,  $\nu = 30^\circ$ . (c) Co<sup>2+</sup> triangular plaquettes used to define the intra- and inter-sublattice scalar spin chiralities  $\chi_s^{\parallel}$  and  $\chi_s^{\perp}$ . (d) Scalar spin chirality contribution from the inter-sublattice plaquettes  $\chi_s^{\perp}$  for the spin configuration in (c) with  $\Delta\phi = 0$ ,  $\Delta\psi = 180^\circ$ . The color of each triangle represents  $\chi_s$  projected onto the  $z$  component of the plaquette and summed over the three plaquettes sharing a vertex plotted as black dots. (e) Same as (d) but with  $\Delta\phi = 180^\circ$ ,  $\Delta\psi = 180^\circ$ .

vanish as  $q \rightarrow 0$ . Thus, the incommensurate modulation is essential for providing a finite local scalar spin chirality in CoNb<sub>3</sub>S<sub>6</sub>.

Due to the opposite canting between sublattices,  $\chi_s^{\perp}$  is much larger than  $\chi_s^{\parallel}$  for the values of  $\nu$  we have found. Although the relative magnitude of the intra- and inter-sublattice hopping integrals are unknown, the effective field produced by  $\chi_s^{\perp}$  will dominate for all feasible values and the qualitative behavior is unchanged by  $\chi_s^{\parallel}$  [15]. In order to visualize  $\chi_s$ , we project  $\chi_s^{\perp}$  onto the  $z$  component of the plaquette normal vectors, shown in Fig. 4(d) and (e) for two different possibilities of the relative phases. In all four cases, the scalar chirality develops an intricate pattern, modulated along both  $\mathbf{Q}_0$  and  $\mathbf{q}$  [15]. Such staggered chirality cannot directly account for the AHE. However, the staggered chirality in the presence of finite spin-orbit coupling may generate a net Berry curvature that can account for the AHE [23]. Alternatively, the structure we have found may play a role in the AHE via the crystal chirality or altermagnetic effects [3, 4, 24, 25]. The finite local chirality should also give rise to nonlinear or nonreciprocal transport [26] in samples with suitably controlled domain structures.

The present findings clarify the microscopic origins of the giant Hall signal in CoNb<sub>3</sub>S<sub>6</sub> and highlight the importance of mesoscale (magnetic domains) in this itinerant frustrated magnet. A noncoplanar magnetic structure may be stabilized through competing exchange interactions [27] or through itinerant frustration in a Kondo lattice model [28–32]. Given that CoS<sub>6</sub> octahedra in CoNb<sub>3</sub>S<sub>6</sub> are disconnected, with distances of 5.75 Å between nearest neighbor Co sites, superexchange is not likely between local Co moments and a Kondo lattice pic-

ture is more natural. Such a mechanism is also consistent with angle resolved photoemission experiments [33]. In this model, the long wavelength modulation at  $\mathbf{q}$  is due to biquadratic interactions originating from Fermi surface instabilities and giving rise to stripes of scalar chirality similar to our observations [29, 30, 34]. The specific value of  $\mathbf{q}$  depends on precise details of the Fermi surface and chemical potential that are further influenced by intrinsic material factors such as lattice strains or chemical defects, consistent with the sample dependence we have observed. This intrinsic sensitivity of the magnetic modulation also affects the domain structure that will, in turn, influence electronic transport in macroscopic samples.

Indeed, a striking feature of our results is the broken symmetry of the domains and differences between samples with identical thermodynamic characterization and well-ordered Co triangular lattices [15]. We refer to the three possible commensurate wavevectors as  $Q_0$ -domains. For a given  $Q_0$ -domain, the symmetry-allowed directions of  $\mathbf{q}$  form  $q$ -domains. For a given  $Q_0, \mathbf{q}$  pair, the helix chirality  $\chi = \pm 1$  and canting direction  $\pm\nu$  give four types of  $\chi$ -domains. In all samples, we only observed a single  $q$ -domain for a given  $Q_0$ , breaking the expected symmetry between each  $Q_0$ . The  $q$ -domains in sample 3 [blue squares in Fig. 1(c)] break both  $C_6$  rotational and mirror symmetry about (110). The  $q$ -domains in samples 1 and 2, [green circles in Fig. 1(c)] break  $C_6$  rotational symmetry, while retaining mirror symmetry about the (110). This same symmetry-breaking is exhibited by the in-plane orientation of the commensurate component measured from FLPA. Although we did not measure reciprocal space maps on that sample, it has the same sur-

face normal as samples 1 and 2, so we expect it to show the same modulation types. It is thus likely that the in-plane orientation of the commensurate component and the helical modulation wavevector are pinned.

The appearance of distinct  $q$ -domains between two  $Q_0$ -domains in a single sample implicates a symmetry breaking strain field. In helimagnets where competing and anisotropic exchange interactions control the modulation, helical wavevectors often align with the strain direction [35–39]. Similarly, small strains can modify the Fermi surface and break degeneracies between nesting vectors in itinerant magnets [40, 41]. The domain selection in samples 1 and 2 can thus naturally be explained by a residual strain along the (110) surface normal that favors  $\mathbf{q}$  more closely aligned with (110) [42]. However, in sample 3, the modulations at  $(\frac{1}{2}00)$  and  $(0\frac{1}{2}0)$  are not along symmetry-equivalent directions and these two peaks cannot be described as separate domains of the same structure. In this sample, the surface normal is tilted away from (110), possibly giving rise to a rotated residual strain that may stabilize the transverse modulation in one  $Q_0$ -domain. This same rotation in the other  $Q_0$ -domain would place the modulation closer to the longitudinal direction ( $q_{\parallel}$ ), which may be unstable.

The two types of  $\chi$ -domains we have identified in  $\text{CoNb}_3\text{S}_6$  provide a microscopic picture for the chiral *micro* and *macro* domains [10], which respectively require field-cooling with 0.1 T and 8 T to align. We observed a finite CD after zero-field cooling that must arise from an unbalanced population of  $\chi$ -domains in the absence of any external symmetry-breaking perturbation, suggesting that magnetic chirality may be coupled to structural chirality [43–45]. Field cooling under a 0.1 T field alters the CD at both  $Q_0$  and  $Q_0 \pm \mathbf{q}$ , consistent with chiral microdomains that arise from spin canting [15].

While the AHE in  $\text{CoNb}_3\text{S}_6$  has been shown to vary greatly with both Co [46] and S [47] stoichiometry, the central importance of the domain structure is implicit through the observed order of magnitude enhancement of the anomalous Hall conductivity in mesoscale samples [10]. Our measurements further highlight and provide a microscopic picture for these domains, demonstrating that quenched in strains can act to give distinct magnetic phenomena between samples with identical stoichiometry. Given the dependence of the magnetic structure on this strain, the AHE may also show a pronounced in-plane anisotropy based on the particular domain populations preferred by the sample geometry. Future work might take advantage of this and employ strain directly to control the symmetry-breaking and tune new phases [48, 49].

In summary, we have discovered a double- $Q$  noncoplanar magnetic structure in  $\text{CoNb}_3\text{S}_6$  exhibiting a staggered scalar spin chirality  $\chi_s$ . The result rules out a uniform scalar chirality as the origin of the anomalous Hall effect, but opens up the possibility for other non-

trivial transport phenomena in this itinerant antiferromagnet. Theoretical work is needed to understand the mechanism underlying this magnetic structure and its impact on transport properties. On the other hand, the magnetic domain pattern reveals a potential tunability of the magnetic modulation through lattice strain that opens up new avenues for controlling the coupling between magnetic order and electronic transport in itinerant antiferromagnets.

## ACKNOWLEDGEMENTS

We are grateful to Cristian Batista for helpful discussions and comments on this manuscript. Work at Brown University was supported by the U.S. Department of Energy, Office of Science, Office of Basic Energy Sciences, under Award Number DE-SC0021265. This work was carried out with the support of Diamond Light Source, beamline I10 under proposal numbers MM30765 and MM30768. We thank Mark Sussmuth for technical support at I10.

---

\* Corresponding author: [kemp\\_plumb@brown.edu](mailto:kemp_plumb@brown.edu)

- [1] C. Sang-Wook and X. Xianghan, *NPJ Quantum Materials* **7**, [10.1038/s41535-022-00447-5](https://doi.org/10.1038/s41535-022-00447-5) (2022).
- [2] S. Nakatsuji and R. Arita, *Annual Review of Condensed Matter Physics* **13**, 119 (2022).
- [3] L. Šmejkal, J. Sinova, and T. Jungwirth, *Phys. Rev. X* **12**, 031042 (2022).
- [4] L. Šmejkal, J. Sinova, and T. Jungwirth, *Phys. Rev. X* **12**, 040501 (2022).
- [5] M. Fiebig, T. Lottermoser, D. Meier, and M. Trassin, *Nature Reviews Materials* **1**, 1 (2016).
- [6] H. Watanabe and Y. Yanase, *Phys. Rev. B* **98**, 245129 (2018).
- [7] S. S. P. Parkin and R. H. Friend, *Philosophical Magazine B* **41**, 65 (1980).
- [8] L. S. Xie, S. Husremović, O. Gonzalez, I. M. Craig, and D. K. Bediako, *Journal of the American Chemical Society* **144**, 9525 (2022).
- [9] N. J. Ghimire, A. Botana, J. Jiang, J. Zhang, Y.-S. Chen, and J. Mitchell, *Nat. Commun.* **9**, 1 (2018).
- [10] G. Terasini, E. Martino, N. Ubrig, N. J. Ghimire, H. Berger, O. Zaharko, F. Wu, J. F. Mitchell, I. Martin, L. Forró, and A. F. Morpurgo, *Phys. Rev. Research* **2**, 023051 (2020).
- [11] S. S. P. Parkin, E. A. Marseglia, and P. J. Brown, *Journal of Physics C: Solid State Physics* **16**, 2765 (1983).
- [12] K. Lu, A. Murzabekova, S. Shim, J. Park, S. Kim, L. Kish, Y. Wu, L. DeBeer-Schmitt, A. A. Aczel, A. Schleife, N. Mason, F. Mahmood, and G. J. MacDougall, [arXiv 10.48550/arxiv.2212.14762](https://arxiv.org/abs/10.48550/arxiv.2212.14762) (2022).
- [13] H. Takagi, R. Takagi, S. Minami, T. Nomoto, K. Ohishi, M.-T. Suzuki, Y. Yanagi, M. Hirayama, N. Khanh, K. Karube, *et al.*, *Nature Physics* , 1 (2023).

- [14] A. Zhang, K. Deng, J. Sheng, P. Liu, S. Kumar, K. Shimada, Z. Jiang, Z. Liu, D. Shen, J. Li, *et al.*, arXiv preprint arXiv:2301.12201 (2023).
- [15] See Supplemental Material for sample characterization, additional REXS data, presentation of phase variable dependence of scalar chirality and details of the calculations.
- [16] T. Ueno, K. Yamamoto, H. Matsukura, T. Kusawake, and K. ichi Ohshima, *Science and Technology of Advanced Materials* **6**, 684 (2005), <https://doi.org/10.1016/j.stam.2005.05.007>.
- [17] T. A. W. Beale, T. P. A. Hase, T. Iida, K. Endo, P. Steadman, A. R. Marshall, S. S. Dhesi, G. van der Laan, and P. D. Hatton, *Review of Scientific Instruments* **81**, 073904 (2010).
- [18] H. Wang, P. Bencok, P. Steadman, E. Longhi, J. Zhu, and Z. Wang, *Journal of Synchrotron Radiation* **19**, 944 (2012).
- [19] Y. A. Izyumov, *Soviet Physics Uspekhi* **27**, 845 (1984).
- [20] J. Herrero-Martín, A. N. Dobrynin, C. Mazzoli, P. Steadman, P. Bencok, R. Fan, A. A. Mukhin, V. Skumryev, and J. L. García-Muñoz, *Phys. Rev. B* **91**, 220403 (2015).
- [21] G. Subías, J. Blasco, J. Herrero-Martín, J. A. Rodríguez-Velamazán, M. Valvidares, R. Fan, P. Steadman, and J. García, *Phys. Rev. B* **103**, 184422 (2021).
- [22] S. Wu, Z. Xu, S. C. Haley, S. F. Weber, A. Acharya, E. Maniv, Y. Qiu, A. A. Aczel, N. S. Settineri, J. B. Neaton, J. G. Analytis, and R. J. Birgeneau, *Phys. Rev. X* **12**, 021003 (2022).
- [23] S.-S. Zhang, H. Ishizuka, H. Zhang, G. B. Halász, and C. D. Batista, *Phys. Rev. B* **101**, 024420 (2020).
- [24] L. Šmejkal, R. González-Hernández, T. Jungwirth, and J. Sinova, *Science Advances* **6**, eaaz8809 (2020).
- [25] L. Šmejkal, A. H. MacDonald, J. Sinova, S. Nakatsuji, and T. Jungwirth, *Nature Reviews Materials* **7**, 482 (2022).
- [26] S. Hayami and M. Yatsushiro, *Journal of the Physical Society of Japan* **91**, 094704 (2022).
- [27] O. Heinonen, R. A. Heinonen, and H. Park, *Phys. Rev. Materials* **6**, 024405 (2022).
- [28] I. Martin and C. D. Batista, *Phys. Rev. Lett.* **101**, 156402 (2008).
- [29] Y. Akagi, M. Udagawa, and Y. Motome, *Phys. Rev. Lett.* **108**, 096401 (2012).
- [30] R. Ozawa, S. Hayami, K. Barros, G.-W. Chern, Y. Motome, and C. D. Batista, *Journal of the Physical Society of Japan* **85**, 103703 (2016).
- [31] S. Hayami, R. Ozawa, and Y. Motome, *Phys. Rev. B* **95**, 224424 (2017).
- [32] S. Hayami and Y. Motome, *Journal of Physics: Condensed Matter* **33**, 443001 (2021).
- [33] X. P. Yang, H. LaBollita, Z.-J. Cheng, H. Bhandari, T. A. Cochran, J.-X. Yin, M. S. Hossain, I. Belopolski, Q. Zhang, Y. Jiang, N. Shumiya, D. Multer, M. Lisch, D. A. Usanov, Y. Dang, V. N. Strocov, A. V. Davydov, N. J. Ghimire, A. S. Botana, and M. Z. Hasan, *Phys. Rev. B* **105**, L121107 (2022).
- [34] S. Hayami, *Journal of Magnetism and Magnetic Materials* **513**, 167181 (2020).
- [35] K. Shibata, J. Iwasaki, N. Kanazawa, S. Aizawa, T. Tanigaki, M. Shirai, T. Nakajima, M. Kubota, M. Kawasaki, H. Park, *et al.*, *Nature nanotechnology* **10**, 589 (2015).
- [36] Y. Nii, T. Nakajima, A. Kikkawa, Y. Yamasaki, K. Ohishi, J. Suzuki, Y. Taguchi, T. Arima, Y. Tokura, and Y. Iwasa, *Nature communications* **6**, 8539 (2015).
- [37] A. Chacon, A. Bauer, T. Adams, F. Rucker, G. Brandl, R. Georgii, M. Garst, and C. Pfleiderer, *Phys. Rev. Lett.* **115**, 267202 (2015).
- [38] S. Lee, T. Choi, W. Ratcliff, R. Erwin, S.-W. Cheong, and V. Kiryukhin, *Phys. Rev. B* **78**, 100101 (2008).
- [39] N. S. Gusev, A. V. Sadovnikov, S. A. Nikitov, M. V. Sapozhnikov, and O. G. Udalov, *Phys. Rev. Lett.* **124**, 157202 (2020).
- [40] G. Simutis, J. Küspert, Q. Wang, J. Choi, D. Bucher, M. Boehm, F. Bourdarot, M. Bertelsen, C. N. Wang, T. Kurosawa, *et al.*, *Communications Physics* **5**, 296 (2022).
- [41] P. Canfield, R. Movshovich, R. Robinson, J. Thompson, Z. Fisk, W. Beyersmann, A. Lacerda, M. Hundley, R. Hefner, D. MacLaughlin, F. Trouw, and H. Ott, *Physica B: Condensed Matter* **197**, 101 (1994).
- [42] T. Inami, N. Terada, H. Kitazawa, and O. Sakai, *Journal of the Physical Society of Japan* **78**, 084713 (2009).
- [43] S. Lim, F.-T. Huang, S. Pan, K. Wang, J. Kim, and S.-W. Cheong, preprint (2020).
- [44] K. Du, F.-T. Huang, J. Kim, S. J. Lim, K. Gamage, J. Yang, M. Mostovoy, J. Garlow, M.-G. Han, Y. Zhu, and S.-W. Cheong, *Proceedings of the National Academy of Sciences* **118**, e2023337118 (2021).
- [45] Y. Horibe, J. Yang, Y.-H. Cho, X. Luo, S. B. Kim, Y. S. Oh, F.-T. Huang, T. Asada, M. Tanimura, D. Jeong, and S.-W. Cheong, *Journal of the American Chemical Society* **136**, 8368 (2014).
- [46] S. Mangelsen, P. Zimmer, C. Näther, S. Mankovsky, S. Polesya, H. Ebert, and W. Bensch, *Phys. Rev. B* **103**, 184408 (2021).
- [47] H. Tanaka, S. Okazaki, K. Kuroda, R. Noguchi, Y. Arai, S. Minami, S. Ideta, K. Tanaka, D. Lu, M. Hashimoto, V. Kandyba, M. Cattelan, A. Barinov, T. Muro, T. Sasagawa, and T. Kondo, *Phys. Rev. B* **105**, L121102 (2022).
- [48] S. L. Zhang, A. Bauer, D. M. Burn, P. Milde, E. Neuber, L. M. Eng, H. Berger, C. Pfleiderer, G. van der Laan, and T. Hesjedal, *Nano Letters* **16**, 3285 (2016).
- [49] Y. Okamura, Y. Yamasaki, D. Morikawa, T. Honda, V. Ukleev, H. Nakao, Y. Murakami, K. Shibata, F. Kagawa, S. Seki, T. Arima, and Y. Tokura, *Phys. Rev. B* **96**, 174417 (2017).

# Supplementary Material for Double- $Q$ spin chirality stripes in the anomalous Hall antiferromagnet $\text{CoNb}_3\text{S}_6$

B. Zager,<sup>1</sup> R. Fan,<sup>2</sup> P. Steadman,<sup>2</sup> and K. W. Plumb<sup>1</sup>

<sup>1</sup>*Department of Physics, Brown University, Providence, Rhode Island 02912, USA*

<sup>2</sup>*Diamond Light Source Ltd., Harwell Science and Innovation Campus, Didcot OX11 0DE, United Kingdom*

(Dated: July 11, 2023)

In the following supplemental material, we show reciprocal space maps of the magnetic scattering from samples 1-4, additional characterization of samples 1-4 including heat capacity, magnetic susceptibility, temperature-dependent rocking scans around the magnetic Bragg peaks, and in- and out-of-plane line cuts through both the magnetic and structural Bragg peaks, along with respective correlation lengths. We also show additional linear polarization analysis data and describe the details of the magnetic structure, scalar spin chirality, and REXS calculations.

## I. SAMPLE CHARACTERIZATION

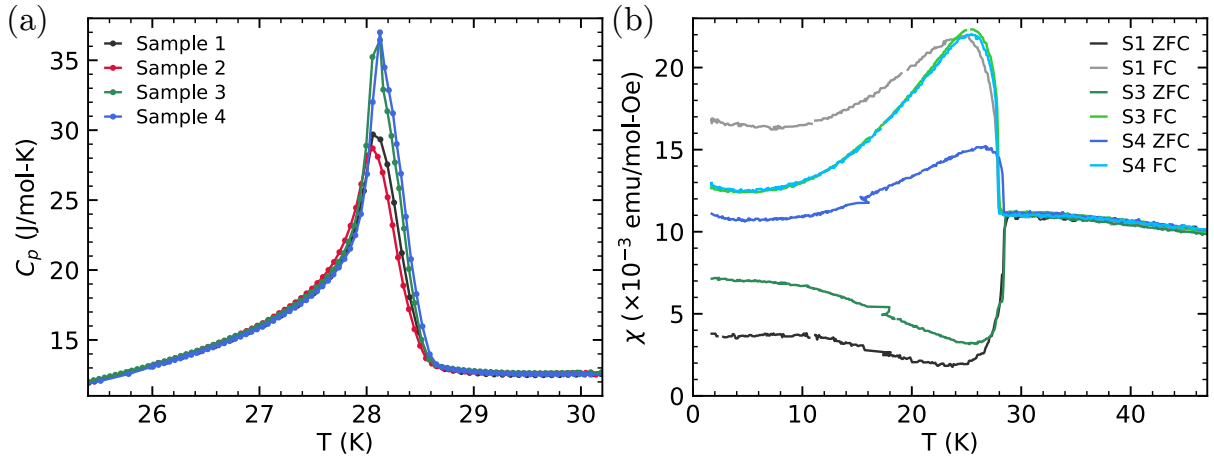


FIG. 1. (a) Heat capacity vs. temperature for samples 1-4. (b) Magnetic susceptibility vs. temperature measured with a 0.1 T field with both zero-field-cooling and field-cooling.

Fig. 1(a) shows the heat capacity of sample 1-4 measured on a Quantum Design Physical Property Measurement System (PPMS). All samples display a clear second-order transition at  $T_N = 28.6$  K. The entropy loss at the transition is slightly greater for samples 3 and 4, indicating possible intrinsic differences between samples.

Fig. 1(b) shows the magnetic susceptibility vs. temperature for samples 1, 3, and 4. Sample 2 was too small to produce a sufficient signal. A constant background  $\chi_0$  was subtracted from each sample, with  $\chi_0 = -2$ , 13, and  $2.3 \times 10^{-3}$  emu/mol-Oe for samples 1, 3, and 4 respectively. All samples show a transition at  $T_N = 28.6$  K with a large splitting between field (FC) and zero field cooling (ZFC), consistent with previous reports [1, 2]. However, the samples display differences between the magnitude of ZFC-FC splitting. This may arise from intrinsic differences between the samples, minute extrinsic impurity phases, or slight misalignment of the magnetic field directions between the samples.

## II. RECIPROCAL SPACE MAPS FOR SAMPLES 1-4

Fig. 2 shows the reciprocal space maps of the magnetic scattering in all four samples. 2(a) and 2(b) show the maps for samples 1 and 2 respectively, which show the same structure. As discussed in the main text, the modulations in the two  $Q_0$ -domains are symmetry-related, but each is missing the other symmetry-allowed  $q$  modulation. 2(c) shows the map for sample 3, as in Fig. 1 (a) of the main text. In this sample, the modulations in the two  $Q_0$ -domains are not symmetry-related. Fig. 2(d) shows the map for sample 4. This sample only shows the commensurate peaks with no satellites. The multiple peaks in the left panel come from crystal mosaic.

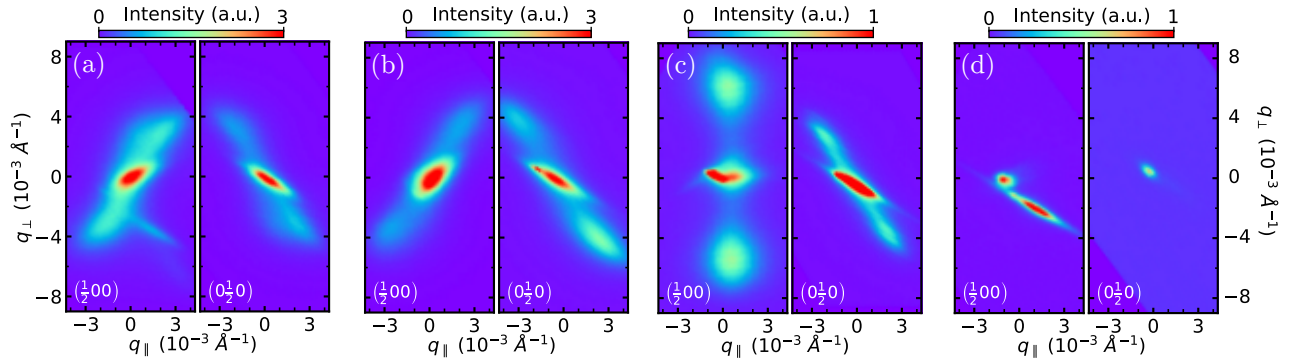


FIG. 2. Reciprocal space maps of the magnetic scattering at  $(\frac{1}{2}00)$  and  $(0\frac{1}{2}0)$  in the  $(HK0)$  plane integrated over 0.003 r.l.u. along the  $L$  direction for (a) sample 1, (b) sample 2, (c) sample 3, and (d) sample 4.

### III. CORRELATION LENGTHS

Fig. 3 shows line cuts along the  $L$  direction for each main and satellite peak in all samples. We use a Lorentzian fit to obtain an out-of-plane correlation length  $\xi_c$ . Fig. 4 shows in-plane transverse line cuts across each peak, which we fit to obtain an in-plane correlation length  $\xi_{ab}$ . For the satellites, the transverse direction is taken with respect to  $\mathbf{q}$ , rather than  $\mathbf{Q}_0 \pm \mathbf{q}$ .

Fig. 5 shows line cuts along the  $L$  direction through the structural peaks measured on the second harmonic (1557 eV) at 30 K. Fig. 6 shows in-plane transverse line cuts through the structural peaks measured on the second harmonic (1557 eV) at 30 K. The structural and magnetic correlation lengths extracted from these fits are summarized in tables I and II below.

These (100)-type structural Bragg peaks arise from the superlattice of intercalated Co ions within the  $\text{NbS}_2$  host layers and the large correlation lengths indicate a well-ordered triangular lattice of Co ions [3] in all samples studied.

TABLE I. Measured correlation lengths for samples 1,2, and 4.

Peak	(100)	(010)	$(\frac{1}{2}00)$	$(\frac{1}{2}\delta 0)$	$(\frac{1}{2}\bar{\delta}0)$	$(0\frac{1}{2}0)$	$(\delta\frac{1}{2}0)$	$(\bar{\delta}\frac{1}{2}0)$
<b>Sample 1</b>								
$\xi_{ab}$ (nm)	563(8)	570(9)	151(14)	93(3)	85(2)	247(7)	107(1)	102(2)
$\xi_c$ (nm)	571(5)	563(5)	212(1)	135(1)	133(1)	265(2)	143(1)	172(1)
<b>Sample 2</b>								
$\xi_{ab}$ (nm)	274(14)	216(12)	136(2)	197(5)	90(2)	99(2)	107(2)	122(2)
$\xi_c$ (nm)	-	182(6)	159(2)	139(2)	112(2)	98(2)	110(2)	97(1)
<b>Sample 4</b>								
$\xi_{ab}$ (nm)	394(8)	474(11)	469(40)	-	-	352(37)	-	-
$\xi_c$ (nm)	195(2)	199(2)	146(3)	-	-	151(4)	-	-

TABLE II. Measured correlation lengths for sample 3.

Peak	(100)	(010)	$(\frac{1}{2}00)$	$(\frac{1}{2}+\delta, -2\delta, 0)$	$(\frac{1}{2}-\delta, 2\delta, 0)$	$(0\frac{1}{2}0)$	$(\delta\frac{1}{2}0)$	$(\bar{\delta}\frac{1}{2}0)$
$\xi_{ab}$ (nm)	274(14)	216(12)	136(2)	197(5)	90(2)	99(2)	107(2)	122(2)
$\xi_c$ (nm)	-	182(6)	159(2)	139(2)	112(2)	98(2)	110(2)	97(1)



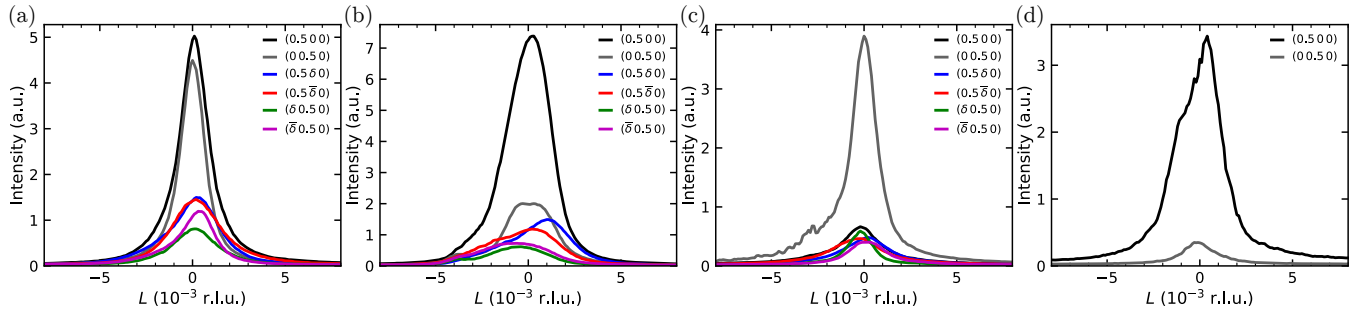


FIG. 3. Line cuts through the magnetic peaks along the  $L$  direction integrated over 0.005 r.l.u. along the  $H$  and  $K$  directions in (a) sample 1, (b) sample 2, (c) sample 3, and (d) sample 4.

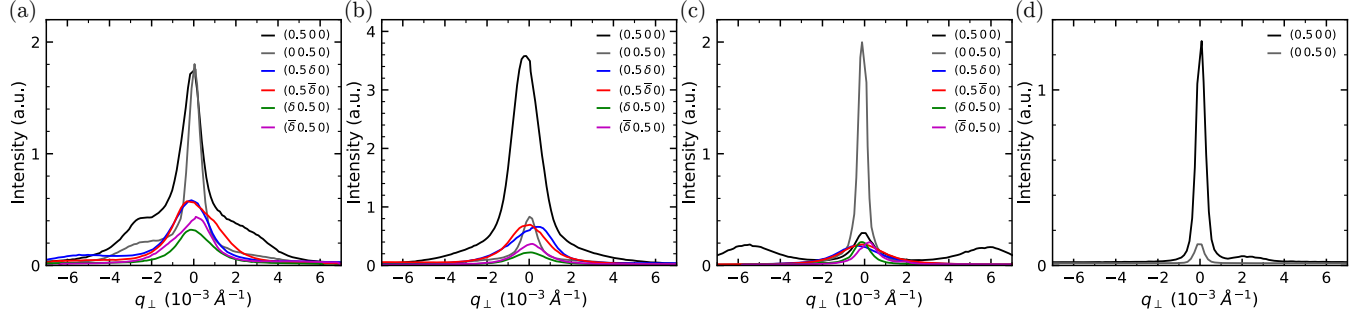


FIG. 4. Line cuts through the magnetic peaks along the transverse direction, integrated over 0.003 r.l.u. along the  $L$  direction and 0.005 r.l.u. along the in-plane longitudinal direction, in (a) sample 1, (b) sample 2, (c) sample 3, and (d) sample 4.

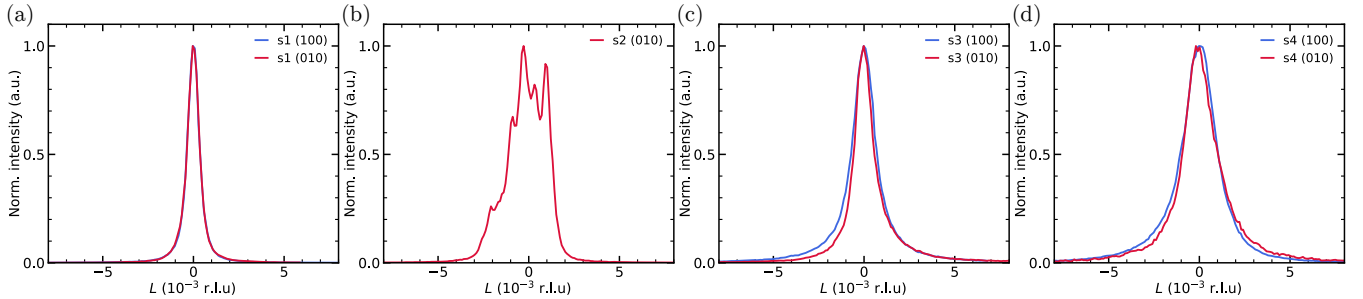


FIG. 5. Line cuts through the structural peaks along the  $L$  direction, integrated over 0.005 r.l.u. along the  $H$  and  $K$  directions, with maximum intensity normalized to 1 in (a) sample 1, (b) sample 2, (c) sample 3, and (d) sample 4, measured on the first harmonic (1557 eV) at 30 K.

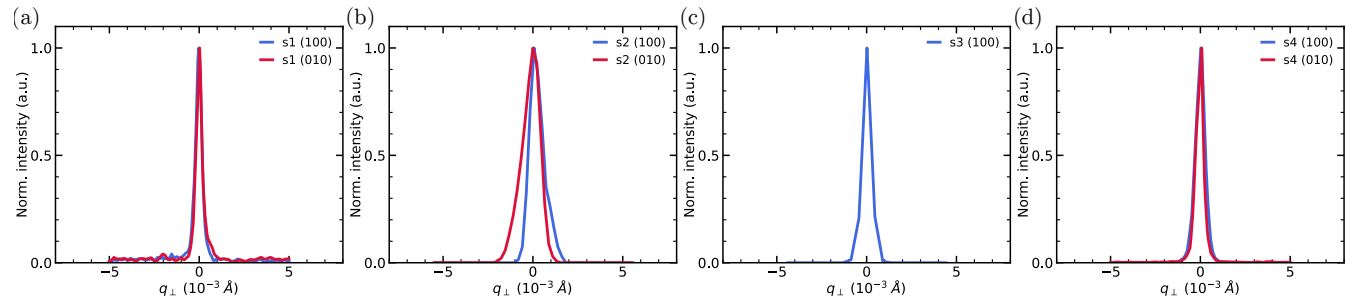


FIG. 6. Line cuts through the structural peaks along the in-plane transverse direction, integrated over 0.003 r.l.u. along the  $L$  direction and 0.005 r.l.u. along the in-plane longitudinal direction, in (a) sample 1, (b) sample 2, (c) sample 3, and (d) sample 4, measured on the first harmonic (1557 eV) at 30 K.

#### IV. TEMPERATURE DEPENDENCE OF MAGNETIC SCATTERING

Fig. 7 shows the temperature dependence of the magnetic scattering for each sample measured from rocking scans on the point detector in  $\pi$  polarization. Above the transition, only the (100) or (010) structural peaks from the 2nd harmonic of the beam remain. The insets show the integrated intensity vs. temperature with the intensity of the structural peak subtracted. Although  $T_N$  as measured through magnetic susceptibility and heat capacity is consistent across all samples, the apparent  $T_N$  in the REXS data varies between samples. This variation arises from a combination of beam heating and variable cooling efficiency for samples mounted on different locations on the sample holder.

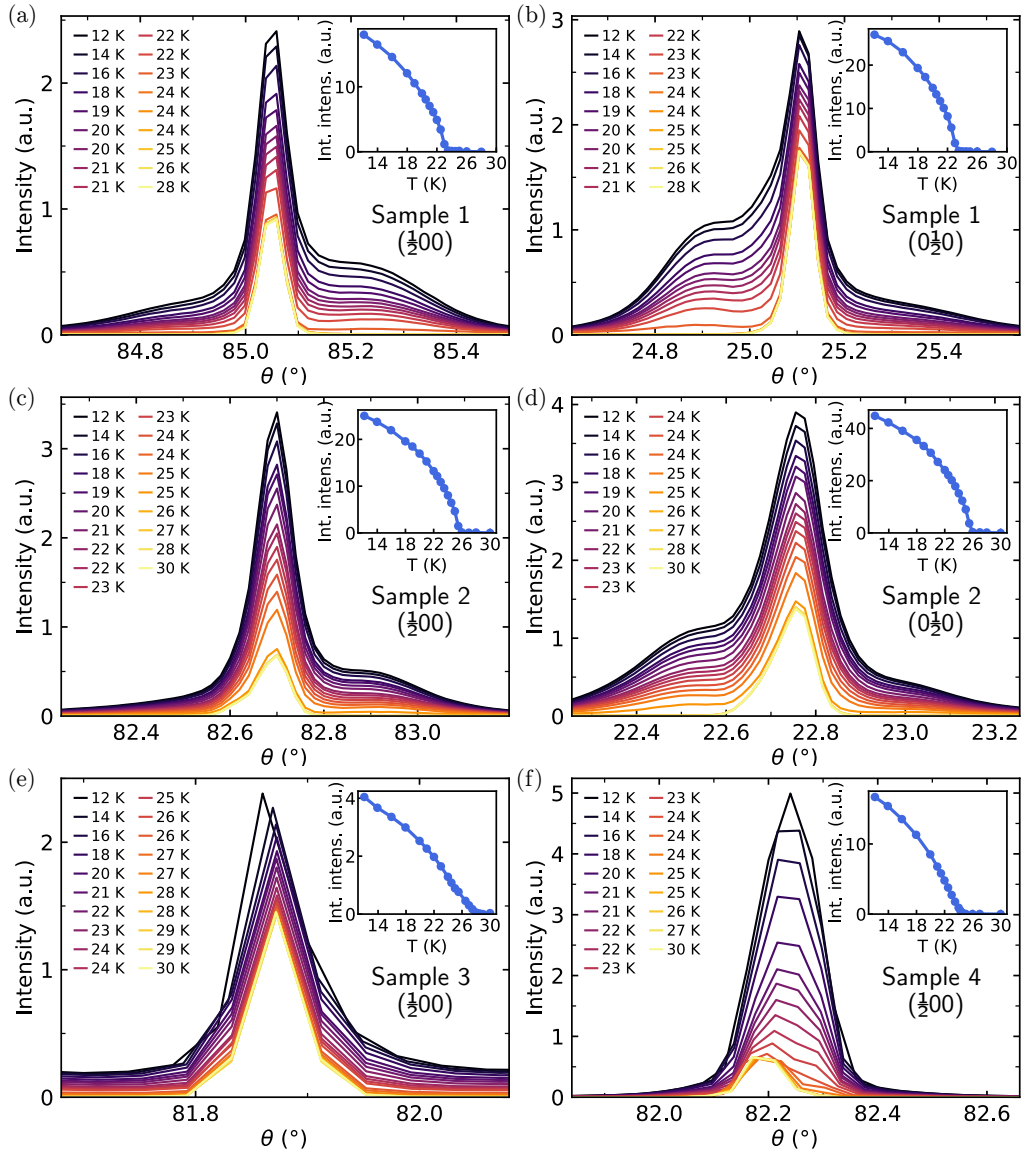


FIG. 7. Temperature dependence of magnetic scattering measured from rocking scans around  $\mathbf{Q}_0$  in  $\pi$  polarization on the point detector for (a) sample 1 ( $\frac{1}{2}00$ ), (b) sample 1 ( $0\frac{1}{2}0$ ), (c) sample 2 ( $\frac{1}{2}00$ ), (d) sample 2 ( $0\frac{1}{2}0$ ), (e) sample 3 ( $\frac{1}{2}00$ ), (f) sample 4 ( $\frac{1}{2}00$ ).

## V. DESCRIPTION OF THE MAGNETIC STRUCTURE

Our data reveal that the magnetic structure of  $\text{CoNb}_3\text{S}_6$  is comprised of two propagation vectors  $\mathbf{Q}_0$  and  $\mathbf{q}$ . There are two possible magnetic structures that may be consistent with this observation. In the main text, we consider the most likely case with magnetic propagation vectors  $\pm\mathbf{Q}_0$  and  $\pm(\mathbf{Q}_0 \pm \mathbf{q})$ . The second possible scenario is a structure with propagation vectors  $\mathbf{Q}_0$  and  $\mathbf{q}$ , giving rise to higher harmonic peaks at  $\mathbf{Q}_0 \pm \mathbf{q}$ . We cannot directly rule out low-angle peaks at  $\mathbf{q} \approx 0$  that were inaccessible in our sample geometry. However, we did not observe any  $\mathbf{Q}_0 \pm n\mathbf{q}$  for  $n > 1$  higher harmonics, which would be expected in this scenario. Furthermore, neutron experiments have not reported any evidence for  $\mathbf{q} \approx 0$  magnetic scattering [4, 5]. We thus consider the more likely case with magnetic propagation vectors  $\pm\mathbf{Q}_0$  and  $\pm(\mathbf{Q}_0 \pm \mathbf{q})$ . The real-space structure is given by a generalized form of the  $2Q$  structure considered in [6],

$$\begin{aligned} \mathbf{m}_n(\mathbf{r}_j) = & \cos(\mathbf{q} \cdot \mathbf{r}_j + \psi_n) \cos(\mathbf{Q}_0 \cdot \mathbf{r}_j + \phi_n) \hat{\mathbf{u}}_n \\ & + \sin(\mathbf{Q}_0 \cdot \mathbf{r}_j + \phi_n) \hat{\mathbf{v}}_n \\ & + \cos(\mathbf{q} \cdot \mathbf{r}_j + \psi_n + \frac{\pi}{2}\chi) \cos(\mathbf{Q}_0 \cdot \mathbf{r}_j + \phi_n) \hat{\mathbf{w}}_n, \end{aligned} \quad (1)$$

where  $n = 1, 2$  labels the sublattices corresponding to the 2 Co sites in the unit cell,  $\chi = \pm 1$  is the chirality,  $\phi_n$  and  $\psi_n$  are the phases on sublattice  $n$  for  $\mathbf{Q}_0$  and  $\mathbf{Q}_0 \pm \mathbf{q}$  respectively, and  $\hat{\mathbf{u}}_n$ ,  $\hat{\mathbf{v}}_n$ , and  $\hat{\mathbf{w}}_n$  are unit vectors, which we assume to be orthogonal to maintain a constant moment size. The magnetic moment on site  $j$  can be expressed as

$$\mathbf{m}(\mathbf{r}_j) = \sum_{\mathbf{Q}} \mathbf{m}_{\mathbf{Q}} e^{i\mathbf{Q}\mathbf{r}_j} \quad (2)$$

where  $\mathbf{m}_{\mathbf{Q}}$  are the Fourier components of the magnetic moments, which, for this structure are given by

$$\begin{aligned} \mathbf{m}_{\mathbf{Q}_0, n} = \mathbf{m}_{-\mathbf{Q}_0, n}^* = & -\frac{i}{2} e^{i\phi_n} \hat{\mathbf{v}}_n \\ \mathbf{m}_{\mathbf{Q}_0 \pm \mathbf{q}, n} = \mathbf{m}_{-\mathbf{Q}_0 \mp \mathbf{q}, n}^* = & \frac{1}{4} e^{i\phi_n \pm i\psi_n} (\hat{\mathbf{u}}_n \pm i\hat{\mathbf{w}}_n). \end{aligned} \quad (3)$$

The precise value of  $\phi_n$  affects the real-space spin structure, ruling out  $\phi_n = \frac{\pi}{2}n$  ( $n = 0, 1, 2, \dots$ ) for which either the commensurate or incommensurate components of the magnetic structure vanish. The precise value of  $\psi_n$  does not affect the real-space structure, since  $\mathbf{q}$  is incommensurate with the lattice. However, the relative phases  $\Delta\phi = \phi_2 - \phi_1$  and  $\Delta\psi = \psi_2 - \psi_1$  do affect the real-space structure. The unit vectors defining the moment orientations are

$$\begin{aligned} \hat{\mathbf{u}}_n = & \hat{\mathbf{x}} \cos \mu + \hat{\mathbf{y}} \sin \mu \\ \hat{\mathbf{v}}_n = & -\hat{\mathbf{x}} \sin \mu \cos \nu_n + \hat{\mathbf{y}} \cos \mu \cos \nu_n + \hat{\mathbf{z}} \sin \nu_n \\ \hat{\mathbf{w}}_n = & \hat{\mathbf{x}} \sin \mu \sin \nu_n - \hat{\mathbf{y}} \sin \nu_n \cos \mu + \hat{\mathbf{z}} \cos \nu_n \end{aligned} \quad (4)$$

for  $n = 1, 2$ , where  $\hat{\mathbf{x}}, \hat{\mathbf{y}}, \hat{\mathbf{z}}$  are cartesian coordinates with  $\hat{\mathbf{x}}$  along  $a$  and  $\hat{\mathbf{y}}$  in the  $a$ - $b$  plane of the crystallographic cell.  $\mu$  defines the in-plane angle relative to the  $x$ -axis,  $\nu_n$  defines the out-of-plane canting angle where we assume  $\nu = \nu_1 = -\nu_2$ . The definitions of coordinate frame  $\hat{\mathbf{u}}, \hat{\mathbf{v}}, \hat{\mathbf{w}}$ , and angles  $\mu$  and  $\nu$  are illustrated in Fig. 8.

## VI. CALCULATIONS OF THE RESONANT MAGNETIC X-RAY SCATTERING INTENSITY

The REXS intensity for is  $I_{\epsilon'\epsilon}(\mathbf{Q}) \propto |S_{\epsilon'\epsilon}(\mathbf{Q})|^2$ , where

$$S_{\epsilon'\epsilon}(\mathbf{Q}) = \sum_j e^{i\mathbf{Q}\cdot\mathbf{r}_j} f_j(E) \quad (5)$$

is the structure factor for incident (outgoing) polarization vector  $\epsilon$  ( $\epsilon'$ ), which sums over all Co sites  $j$ , and  $E$  is the x-ray energy. In the dipole approximation, the resonant form factor at atomic site  $j$  is

$$f_j = (\epsilon'^* \cdot \epsilon) F^{(0)} + (\epsilon'^* \times \epsilon) \cdot \mathbf{m}_j F^{(1)} + (\epsilon'^* \cdot \mathbf{m}_j) (\epsilon \cdot \mathbf{m}_j) F^{(2)} \quad (6)$$

where  $\mathbf{m}_j$  is the direction of the magnetic moment on the site and  $F^{(i)}$  are the energy-dependent resonant scattering factors [7]. We observed no intensity in the  $\sigma$ - $\sigma$  channel, so we let  $F^{(0)} = 0$ . The third term gives rise to second-order satellite reflections, which we did not observe, so we let  $F^{(2)} = 0$ . We thus have

$$S_{\epsilon'\epsilon}(\mathbf{Q}) \propto (\epsilon'^* \times \epsilon) \cdot \mathbf{M}(\mathbf{Q}) \quad (7)$$

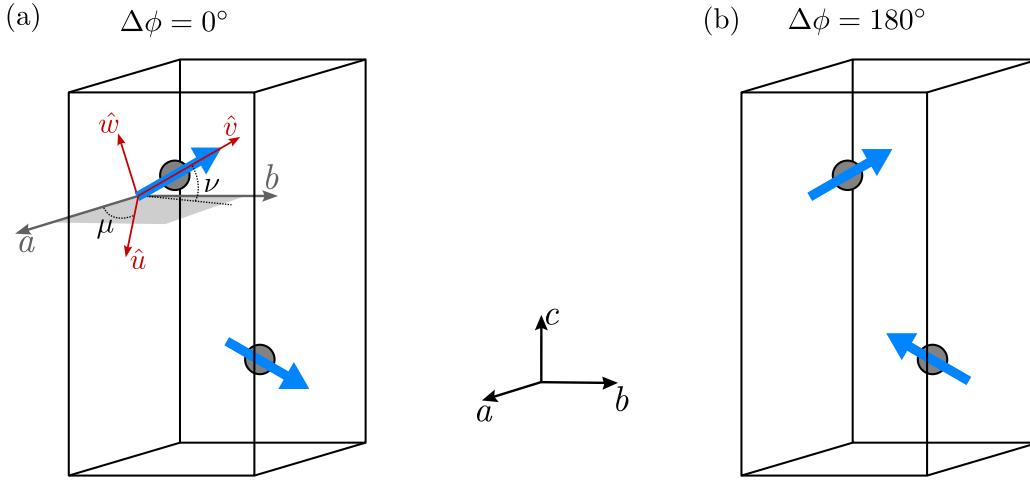


FIG. 8. Fourier component  $m_{\mathbf{Q}_0}$  of the commensurate part of the magnetic structure, showing the in-plane angle  $\mu$  and canting angle  $\nu$  for the phase (a)  $\Delta\phi = 0^\circ$ . (b)  $\Delta\phi = 180^\circ$ .

where  $M(\mathbf{Q})$  is the magnetic structure factor. For the main magnetic reflection at  $\mathbf{Q}_0 = (\frac{1}{2}00)$ ,

$$M(\mathbf{Q}_0) = -\frac{i}{2}e^{i(\frac{2}{3}\pi+\phi_1)}\hat{\mathbf{v}}_1 - \frac{i}{2}e^{i(\frac{1}{3}\pi+\phi_2)}\hat{\mathbf{v}}_2 \quad (8)$$

For the  $\mathbf{q} = (0\delta 0)$  satellites,

$$M(\mathbf{Q}_0 \pm \mathbf{q}) = \frac{1}{4} \left[ ie^{i(\pm\frac{4\pi}{3}\delta+\phi_1)}\hat{\mathbf{u}}_1 \mp \chi e^{i(\pm\frac{4\pi}{3}\delta+\phi_1)}\hat{\mathbf{w}}_1 + ie^{i(\pm\frac{2\pi}{3}\delta+\phi_2)}\hat{\mathbf{u}}_2 \mp \chi e^{i(\pm\frac{2\pi}{3}\delta+\phi_2)}\hat{\mathbf{w}}_2 \right] \quad (9)$$

For the  $\mathbf{q} = (\delta, -2\delta, 0)$  satellites,

$$M(\mathbf{Q}_0 \pm \mathbf{q}) = \frac{1}{4} \left[ ie^{i(\phi_1 \mp 2\pi\delta)}\hat{\mathbf{u}}_1 \mp \chi e^{i(\phi_1 \mp 2\pi\delta)}\hat{\mathbf{w}}_1 + ie^{i\phi_2}\hat{\mathbf{u}}_2 \mp \chi e^{i\phi_2}\hat{\mathbf{w}}_2 \right] \quad (10)$$

### A. Full linear polarization analysis (FLPA)

Let  $\hat{\mathbf{Q}}$  be the unit vector along the direction of the scattering vector  $\mathbf{Q}$  and let  $\hat{\mathbf{Q}}_\perp$  be a direction perpendicular to  $\hat{\mathbf{Q}}$  within the  $(HK0)$  scattering plane. The directions of the incident and scattered beam are given by

$$\begin{aligned} \hat{\mathbf{k}} &= \hat{\mathbf{Q}}_\perp \cos \theta + \hat{\mathbf{Q}} \sin \theta \\ \hat{\mathbf{k}}' &= \hat{\mathbf{Q}}_\perp \cos \theta - \hat{\mathbf{Q}} \sin \theta. \end{aligned} \quad (11)$$

where  $\theta$  is half of the Bragg angle [8]. We can represent the polarization in the basis  $\boldsymbol{\sigma}$  (perpendicular to the scattering plane) and  $\boldsymbol{\pi}$  (parallel to the scattering plane), given by

$$\begin{aligned} \boldsymbol{\sigma} &= \boldsymbol{\sigma}' = (\hat{\mathbf{k}} \times \hat{\mathbf{k}}') / \sin(2\theta) \\ \boldsymbol{\pi} &= \hat{\mathbf{k}} \times \boldsymbol{\sigma} \\ \boldsymbol{\pi}' &= \hat{\mathbf{k}}' \times \boldsymbol{\sigma}. \end{aligned} \quad (12)$$

The linear polarization vector is then given by

$$\begin{aligned} \boldsymbol{\epsilon} &= \boldsymbol{\sigma} \cos \alpha + \boldsymbol{\pi} \sin \alpha \\ \boldsymbol{\epsilon}' &= \boldsymbol{\sigma}' \cos \eta + \boldsymbol{\pi}' \sin \eta \end{aligned} \quad (13)$$

The REXS intensity can then be calculated using Eq. 7. As expected for the  $E1$ - $E1$  contribution to magnetic scattering, the  $\sigma$ - $\sigma'$  intensity is always zero. The  $\sigma$ - $\pi'$  and  $\pi$ - $\sigma'$  intensity originates from the component of the moment in the crystallographic  $a$ - $b$  (basal) plane and the  $\pi$ - $\pi'$  intensity arises from the out-of-plane component. Fig. 9 shows the complete FLPA dataset as a colormap along with the model calculations. We note that the analyzer reduces the intensity by two orders of magnitude, so the signal at the satellites was too weak to carry out FLPA.

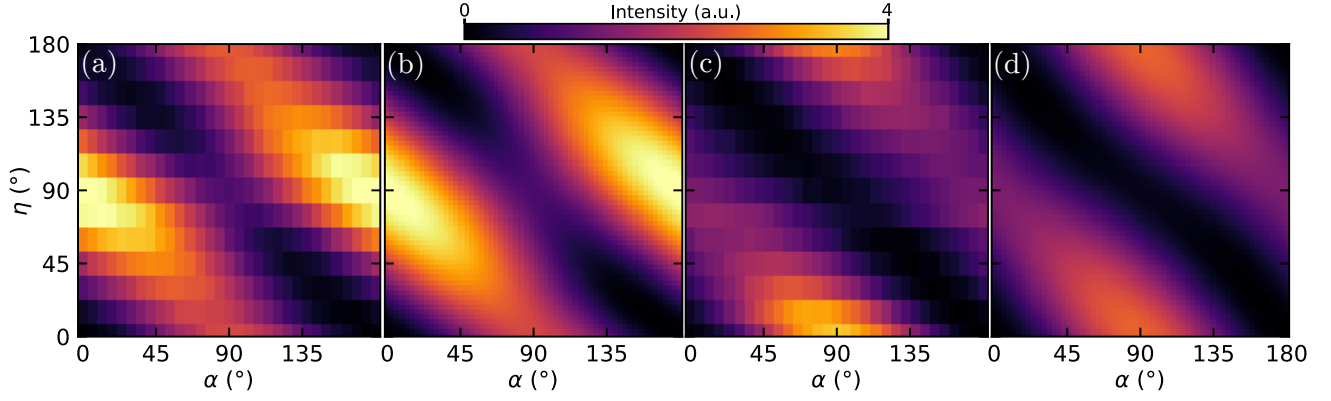


FIG. 9. (a) FLPA data at  $(\frac{1}{2}00)$ . (b) FLPA calculation at  $(\frac{1}{2}00)$  using the parameters from the main text. (c) FLPA data at  $(0\frac{1}{2}0)$ . (d) FLPA calculation at  $(0\frac{1}{2}0)$  using the parameters from the main text.

### B. Circular dichroism

For circularly polarized x-rays  $\epsilon_{\pm} = \frac{1}{\sqrt{2}}(\sigma \mp i\pi)$ , the intensity  $I_{\pm} = I_{\pm\pm} + I_{\mp\pm}$  is [9]

$$I_{\pm} = \frac{1}{2}(|S_{\sigma'\sigma}|^2 + |S_{\sigma'\pi}|^2 + |S_{\pi'\sigma}|^2 + |S_{\pi'\pi}|^2) \pm \text{Im}(S_{\sigma'\sigma}S_{\sigma'\pi}^* + S_{\pi'\sigma}S_{\pi'\pi}^*), \quad (14)$$

The circular dichroism is

$$I_+ - I_- = 2 \text{Im}(S_{\pi'\sigma}S_{\pi'\pi}^*), \quad (15)$$

where we have assumed  $S_{\sigma'\sigma} = 0$ . Thus the condition for finite CD is a finite structure factor for both  $\sigma$ - $\pi'$  and  $\pi$ - $\pi$ . This requires both an in- and out-of-plane spin component, which indicates that the modulation is helical and confirms the FLPA results that the commensurate component must be noncollinear. Fig. 10 shows the calculated CD as a function of canting angle  $\nu$  at  $\mu = 109^\circ$ .

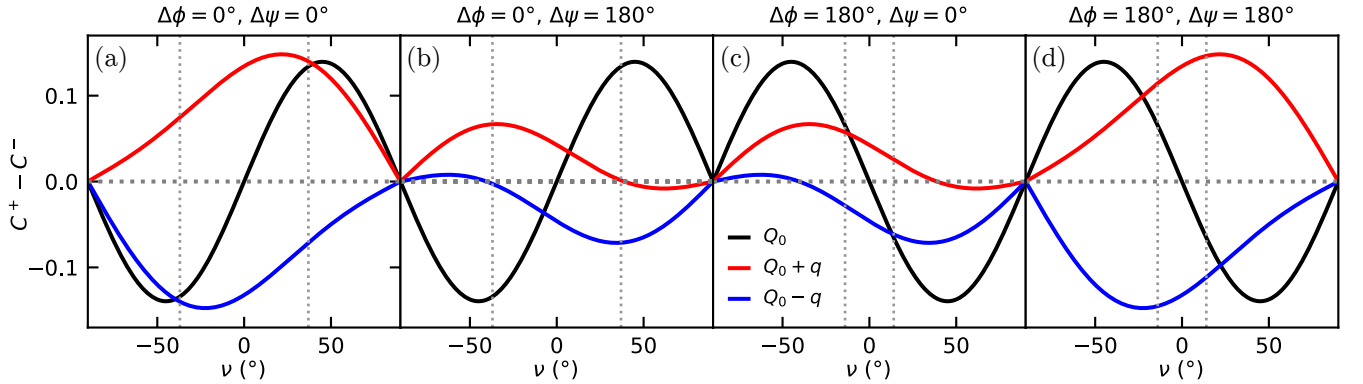


FIG. 10. Dependence of the CD on the canting angle  $\nu$  at  $\mathbf{Q}_0 = (\frac{1}{2}00)$  and  $\mathbf{Q}_0 \pm (0\delta 0)$  for each of the four phase combinations with  $\mu = 109^\circ$ . The vertical dashed lines show the value of  $\nu$  determined from FLPA for each choice of phases.

The magnetic structure determined from FLPA is consistent with the CD-REXS results. The condition for CD at  $\mathbf{Q}_0$  is finite intensity in both  $\sigma$ - $\pi$  and  $\pi$ - $\pi$ , which arises from the noncollinear moments with both in- and out-of-plane components. The CD at  $\mathbf{Q}_0 \pm \mathbf{q}$  requires a helical structure or a more complex chiral modulation.

We note that there is a contribution to the CD from the structural peaks on second harmonic, which is forbidden for Thomson scattering. This is due to the imperfect circular polarization of the 2nd harmonic, giving unequal combinations of  $\sigma$  and  $\pi$  polarization between  $C+$  and  $C-$  [10].

## VII. SCALAR SPIN CHIRALITY

The scalar spin chirality on a triangular plaquette of sites  $\mathbf{r}_i$ ,  $\mathbf{r}_j$ , and  $\mathbf{r}_k$  with moments  $\mathbf{m}_i$ ,  $\mathbf{m}_j$ , and  $\mathbf{m}_k$  is defined as  $\chi_s = \mathbf{m}_i \cdot (\mathbf{m}_j \times \mathbf{m}_k)$ . The effective magnetic field felt by a conduction electron passing over this plaquette is  $\mathbf{b} \propto t \chi_s \hat{\mathbf{n}}$ , where  $\hat{\mathbf{n}}$  is the plaquette normal vector and  $t = t_{ij}t_{jk}t_{ki}$  is the hopping integral around the loop  $i \rightarrow j \rightarrow k \rightarrow i$ . The lattice of magnetic Co sites in  $\text{CoNb}_3\text{S}_6$  consists of two triangular sublattices. Thus, there are intra-sublattice plaquettes formed by three sites in the same basal plane, as well as inter-sublattice plaquettes formed by two sites from a given sublattice and one site from the opposite one. We denote the intra- and inter-sublattices contributions as  $\chi_s^\parallel$  and  $\chi_s^\perp$  respectively. For intra-sublattice plaquettes,

$$\chi_s^\parallel(\mathbf{r}) = \sin\left(\frac{\pi\chi}{2}\right) \sin \Phi_{\mathbf{r}} \cos^2 \Phi_{\mathbf{r}} [\sin(\alpha + \beta) - \sin \alpha - \sin \beta], \quad (16)$$

where  $\mathbf{q} = (\alpha\beta 0)/2\pi$  is the modulation wavevector,  $\Phi_{\mathbf{r}} = \mathbf{Q}_0 \cdot \mathbf{r} + \phi_n$ , and  $\chi$  is the helix chirality. This vanishes everywhere if either  $\alpha = 0$  or  $\beta = 0$  and is independent of  $\psi$ ,  $\mu$ , and  $\nu$ . We can see that  $\chi_s^\parallel$  has a fixed magnitude at all positions but oscillates in sign along the direction of  $\mathbf{Q}_0$ . The sum of  $\chi_s^\parallel$  for the two sublattices is shown in Fig. 11. Since the sites on each sublattice are offset along the direction of  $\mathbf{Q}_0$ , there is a phase difference in the contribution from each sublattice. This causes some interference, seen as the black regions of vanishing  $\chi_s$ .

$\chi_s^\perp$  does not vanish for any particular direction of  $\mathbf{q}$ , but vanishes as  $q \rightarrow 0$ . Similarly to  $\chi_s^\parallel$ ,  $\chi_s^\perp$  oscillates in sign along  $\mathbf{Q}_0$ , but also oscillates along  $\mathbf{q}$ . The amplitude of these oscillations depends on  $\nu$ , with no oscillations for  $\nu = 0$ . The precise pattern of  $\chi_s^\perp$  depends on the choice of phase differences  $\Delta\phi$  and  $\Delta\psi$ , plotted in Fig. 12. Here we show the value of  $\chi_s^\perp$  projected onto the  $z$ -component of the plaquette normal and summed over each group of three edge-sharing inter-sublattice plaquettes.

The pattern along  $\mathbf{Q}_0$  depends on the sum  $\Delta\phi + \Delta\psi$  and the pattern along  $\mathbf{q}$  depends only on  $\Delta\psi$ . For  $\Delta\phi + \Delta\psi = 0^\circ$  or  $360^\circ$ ,  $\chi_s^\perp$  forms a stripe pattern. For  $\Delta\phi + \Delta\psi = 180^\circ$   $\chi_s^\perp$  forms a checkerboard pattern. For  $\Delta\psi = 0^\circ$ ,  $\chi_s^\perp$  oscillates about zero along  $\mathbf{q}$ . For  $\Delta\psi = 180^\circ$ ,  $\chi_s^\perp$  oscillates in magnitude along  $\mathbf{q}$  without passing through zero with an amplitude that increases with increasing  $\nu$ .

Although the magnitude of  $\chi_s^\perp$  is much greater than that of  $\chi_s^\parallel$ , the relative magnitude of the effective field  $\mathbf{b}$  is more relevant. We have already projected  $\chi_s^\perp$  onto the  $z$ -component of the plaquette normal vectors, so we only need to consider the relative hopping integrals around each type of plaquette,  $t_\parallel = t^3$  and  $t_\perp = t'^2 t$ , where  $t$  and  $t'$  are the in- and out-of-plane hopping integrals along a single bond. Since the ratio of bond lengths  $a'/a \approx 1.2 \text{ \AA}$ , we expect  $t' < t$ . Thus, the relative contribution of  $\chi_s^\perp$  will be reduced by a factor of  $t'^2/t^2$ . However, the qualitative behavior of  $\mathbf{b}$  remains unaffected.

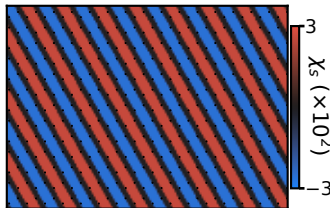


FIG. 11. Scalar spin chirality  $\chi_s^\parallel$  from the intra-sublattice plaquettes, summed over both sublattices for the structure  $\mathbf{Q}_0 = (\frac{1}{2}00)$  and  $\mathbf{q} = (-\delta, 2\delta, 0)$ ,  $\delta = 0.053$  r.l.u.,  $\phi = 45^\circ$ .

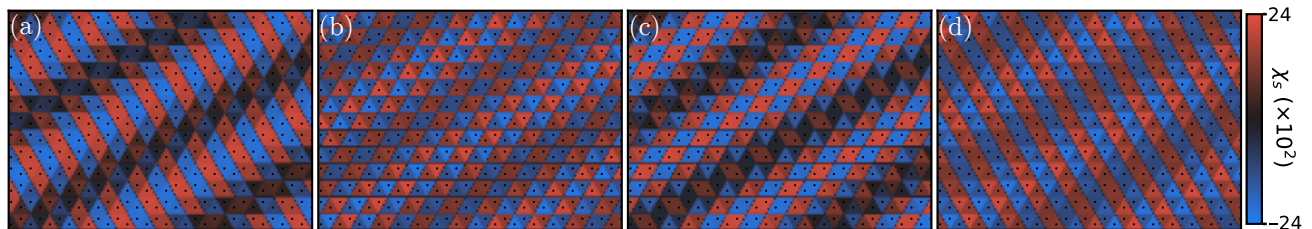


FIG. 12. Scalar spin chirality  $\chi_s^\perp$  from the inter-sublattice plaquettes projected on the  $z$ -component of the plaquette normal vectors for the structure with  $\mathbf{Q}_0 = (\frac{1}{2}00)$  and  $\mathbf{q} = (-\delta, 2\delta, 0)$ ,  $\delta = 0.053$  r.l.u. (larger than the observed value of  $\delta = 0.003$  r.l.u. to simplify visualization),  $\phi = 45^\circ$ ,  $\mu = 110^\circ$ ,  $\nu = 30^\circ$  (a)  $\Delta\phi = 0^\circ$ ,  $\Delta\psi = 0^\circ$ . (b)  $\Delta\phi = 0^\circ$ ,  $\Delta\psi = 180^\circ$ . (c)  $\Delta\phi = 180^\circ$ ,  $\Delta\psi = 0^\circ$ . (d)  $\Delta\phi = 180^\circ$ ,  $\Delta\psi = 180^\circ$ .

- 
- [1] N. J. Ghimire, A. Botana, J. Jiang, J. Zhang, Y.-S. Chen, and J. Mitchell, *Nat. Commun.* **9**, 1 (2018).
  - [2] H. Tanaka, S. Okazaki, K. Kuroda, R. Noguchi, Y. Arai, S. Minami, S. Ideta, K. Tanaka, D. Lu, M. Hashimoto, V. Kandyba, M. Cattelan, A. Barinov, T. Muro, T. Sasagawa, and T. Kondo, *Phys. Rev. B* **105**, L121102 (2022).
  - [3] T. Ueno, K. Yamamoto, H. Matsukura, T. Kusawake, and K. ichi Ohshima, *Science and Technology of Advanced Materials* **6**, 684 (2005), <https://doi.org/10.1016/j.stam.2005.05.007>.
  - [4] S. S. P. Parkin, E. A. Marseglia, and P. J. Brown, *Journal of Physics C: Solid State Physics* **16**, 2765 (1983).
  - [5] K. Lu, A. Murzabekova, S. Shim, J. Park, S. Kim, L. Kish, Y. Wu, L. DeBeer-Schmitt, A. A. Aczel, A. Schleife, N. Mason, F. Mahmood, and G. J. MacDougall, arXiv [10.48550/arxiv.2212.14762](https://arxiv.org/abs/10.48550/arxiv.2212.14762) (2022).
  - [6] O. Heinonen, R. A. Heinonen, and H. Park, *Phys. Rev. Materials* **6**, 024405 (2022).
  - [7] J. P. Hill and D. F. McMorrow, *Acta Crystallographica Section A* **52**, 236 (1996).
  - [8] M. W. Haverkort, N. Hollmann, I. P. Krug, and A. Tanaka, *Phys. Rev. B* **82**, 094403 (2010).
  - [9] A. M. Mulders, S. M. Lawrence, A. J. Princep, U. Staub, Y. Bodenthin, M. García-Fernández, M. Garganourakis, J. Hester, R. Macquart, and C. D. Ling, *Phys. Rev. B* **81**, 092405 (2010).
  - [10] H. Wang, P. Bencok, P. Steadman, E. Longhi, J. Zhu, and Z. Wang, *Journal of Synchrotron Radiation* **19**, 944 (2012).